ESR, XPS, and thin-film RRDE characterization of nano structured carbon materials for catalyst support in PEM fuel cells

Mikkel Juul Larsen[1], Eivind M. Skou*

Institute of Chemical Engineering, Biotechnology and Environmental Technology, University of Southern Denmark, Niels Bohrs Allé 1, DK-5230 Odense M, Denmark

ABSTRACT

With the aim of investigating possible connections between structural properties and electrocatalytic characteristics in the oxygen reduction reaction (ORR) for carbon materials with prospective use as catalyst support in polymer electrolyte membrane fuel cells (PEMFC), various carbon samples were examined by electron spin resonance (ESR) spectroscopy, X-ray photoelectron spectroscopy (XPS), and rotating ring–disc electrode (RRDE) technique. The investigated materials were raw and heat-treated carbon black (CB), activated few-walled carbon nanotubes (FWCNTs), functionalized and graphitized multi-walled carbon nanotubes (GMWCNTs), and graphitized carbon nanofibres (CNF). ESR spectroscopy using MgO internal reference showed that raw CB has the highest defect concentration; graphitized CB, GMWCNTs, and CNF are structurally much more perfect; and FWCNTs are in between. XPS analyses revealed oxygen contents of 0.5–3.9 at%, with hydroxyl-functionalized GMWCNT having the highest content. Thin-film RRDE experiments showed that the activity towards ORR for this latter material is remarkably high, and that about 75% of the oxygen is reduced by a peroxide pathway. For the other samples this pathway accounts for 25–75%. However, no significant ORR activity occurred above 0.2 V vs. dynamic hydrogen electrode. Peroxide formation on carbon is thus an issue on the hydrogen (anode) side of a fuel cell where crossover oxygen may be present.

1. Introduction

Recently a variety of nanostructured carbon materials have attracted a lot of interest as alternatives to carbon black (CB) for supporting the noble-metal catalyst nanoparticles in polymer electrolyte membrane fuel cell (PEMFC) electrodes [1,2]. The conventionally used CBs are prone to electrochemical oxidation during long-term operation of the fuel cell due to their defective structures with abundant reactive sites [3,4]. Such corrosion of the catalyst support is a critical durability issue as it can lead to severe performance losses and reduced lifetime [5]. Carbon types with a more graphitic character are more corrosion resistant since they mainly expose graphite basal planes and hence fewer edges and defects that can be oxidatively attacked [4,6]. The prospective alternatives include graphitized CBs, carbon nanotubes (CNTs), and carbon nanofibres (CNFs). Graphitization of the carbon support has been demonstrated to improve the stability towards corrosion in PEMFCs [6,7], and significantly higher resistance to electrochemical oxidation than that of CBs has been reported for CNTs in

acidic environment [3,8–10] and for CNF as support in a PEMFC membrane–electrode assembly (MEA) [11]. In addition, the resistance to thermal degradation has proved to be higher for CNT and CNF than for CB [12], and the thermal stabilities of platinum-loaded CNT, CNF, and graphitized CB are all higher than that of pristine CB loaded with Pt [12,13].

It has been demonstrated that it is possible to make catalysts with good dispersion of Pt nanoparticles based on the above-mentioned alternative support materials [1,11,14,15]. However, due to their more graphitic character an activation of their surfaces may be necessary in order to achieve the satisfactory catalyst dispersion on these. This can, e.g., be done by the use of aggressive acid oxidants (HNO$_3$ and/or H$_2$SO$_4$), which results in the creation of functional groups such as hydroxyl, carboxyl, and carbonyl on the surface [1]. These groups facilitate the interaction between the support surface and the catalyst or its precursor, thus leading to better anchoring of catalyst nanoparticles. Various activation treatments are possible, and they play an important role not only for the quality of the catalyst dispersion, but also with respect to the durability and electrochemical behaviour of the support itself.

It is thus desirable to know the properties of the new carbon materials themselves and those introduced by their activation treatments. In this connection surface-group analysis is an important tool, and it can be valuable in the tuning of the activation

process. Furthermore, from a survey of the magnetic properties useful structural information can be derived. Another important property to elucidate in order to assess the suitability of a carbon type and/or treatment is the electrocatalytic characteristics of the material, especially with respect to its possible promotion of the formation of unwanted reaction side products. In PEMFCs peroxide side products are detrimental as they are assumed to play a role in the degradation of the electrolyte membrane [5,16–18]. Although, compared to the highly active Pt, carbon is not an efficient catalyst for the electrochemical oxygen reduction reaction (ORR) in acidic environments [19], it is well-established that at carbon surface sites the proportion of the reacting oxygen that is converted into peroxide is very large [20,21] and that particularly at low potentials appreciable amounts of peroxide species may be generated on carbon in the ORR [22]. ORR at low potentials (~0 V) and resulting formation of hydrogen peroxide (E^θ = 0.67 V) occurs on fuel-cell anodes fed by trace oxygen that has crossed through the electrolyte from the cathode [23,24] or when air-bleeding is used at the anode. In hydrogen fuel cells—unless operated at high load—the potential of the cathode (~0.65 to 0.70 V) is too high for significant hydrogen-peroxide formation to take place there, and thus the major generation of peroxide species in the MEA may occur at the anode even though the concentration of oxygen is much lower than that at the cathode [23,25]. For the above reasons the carbon support material in the anode may thus contribute noticeably to the total peroxide generation in the MEA. The mechanism for oxygen reduction on a carbon material is controlled to a large extent by the surface structure [4,20], and thus the extent of peroxide generation is presumed to dependent considerably on the type of carbon and the possible surface modifications made to it. Hence it is advantageous to know the ability of a novel carbon support material to promote the formation of peroxide.

In this work we characterize several new candidate catalyst–support materials in the form of a unique range of different types of carbon subjected to different treatments. The objective is to investigate structural properties related to electron-spin characteristics and surface oxygen functionalities as well as the possible effects of these properties on the electrocatalytic activity of the carbons for the reduction of oxygen and the formation of peroxide. For this purpose we set up and apply methods for performing electron spin resonance (ESR) spectroscopy, X-ray photoelectron spectroscopy (XPS), and rotating ring–disc electrode (RRDE) analyses of carbon samples and present comparative results from the broad collection of carbon materials.

2. Theory and background

Basically two types of electronic spins exist in graphene-based carbon materials: one arising from localized spin species and another from conduction electrons [26,27]. The localized spins are present at structural imperfections and can be due to various stable radical species in the form of, e.g., surface groups or resonance-stabilized aromatic π radicals at zigzag-type edges and defects in the graphene sheets [26,28,29]. The conduction electrons are itinerant π electrons in the conduction band of carbon atoms in graphitic nanocrystallites or walls. In materials characterized by high structural disorder the localized spins are abundant, whereas spin from conduction carriers is predominant in more graphitic materials [26]. ESR spectroscopy is a useful technique for the characterization of carbon samples with respect to their degree of perfection, since the spin types give rise to different signals in the ESR spectrum [4]. Due to the differences in the chemical environment of the electrons of the two spin types their signals have different resonance field values, g. In ESR spectroscopy the g value is obtained according to Eq. (1) from the strength of the magnetic field, B, at the resonance

and the frequency, ν, of the electromagnetic radiation inducing the spin transition [30]:

$$g = \frac{h\nu}{\mu_B B} = \frac{\nu}{B} \cdot 7.14478 \times 10^{-7} \quad \text{G s} \tag{1}$$

where $h = 6.62608 \times 10^{-34}$ J s is the Planck constant and $\mu_B = 9.27402 \times 10^{-28}$ J G^{-1} is the Bohr magneton.

In previous work on quantitative ESR analysis annealed magnesium oxide (MgO) was found to be a suitable substance for internal reference [31]. When MgO powder is mixed with the carbon powder to be investigated, it serves both as a standard for quantification and as a diluting agent preventing signal saturation. Hence suitable ESR samples can be prepared by direct mixing of carbon and MgO at a fixed ratio, and the spin concentration in the carbon material can be compared among different samples by the use of the size of the MgO signal for normalization.

The content of oxygen in the surface layers of carbonaceous materials can be studied by XPS, which is a practical technique for the determination of chemical composition and nature of the chemical bonds [4,32]. If a substantial amount of oxygen species is present, it may be possible to determine the types of these and their relative abundances. This is done by careful analysis of the peaks representing the C 1s and O 1s electrons, respectively. Depending on the type of carbon and its preceding treatment the predominant oxygen functionalities may be hydroxyl, ether, carbonyl, quinone, carboxyl, lactones, or anhydride groups, etc., with the binding energy of the C 1s electrons increasing with higher number of C–O bonds to their host atom and that of the O 1s electrons decreasing [33–35].

RRDE measurements can yield a lot of useful information about the kinetics of electrochemical reactions [36,37]. The usual information from a cyclic voltammogram (CV) of the disc electrode can be supplemented by the information obtained from the simultaneous detection of reaction products by the ring. For electrode materials with prospective use in fuel cells especially the electrocatalytic activity in the ORR and the amount of potentially harmful peroxide species generated in this process are of interest.

The fraction of peroxide, $X_{H_2O_2}$, emitted from the disc electrode during the ORR is calculated by the use of Eq. (2) from the disc (reduction) current, I_D, and the current, I_R, on the ring, which must be held at a potential high enough to oxidize the peroxide species.

$$X_{H_2O_2} = \frac{2I_R/N}{-I_D + (I_R/N)} \tag{2}$$

N is the collection efficiency of the RRDE, which must be determined experimentally.

In order to test a material by the RRDE technique a suitable electrode must be prepared from it on the disc. For this purpose a thin-film method has been developed by Behm and collaborators [22,38]. In this method—intended for the characterization of the ORR on high-surface-area carbon-supported Pt fuel-cell catalysts—an electrode is produced in a two-step drop-coating process, in which the catalyst powder is first deposited on the disc and then coated by a very thin Nafion® layer. The use of very low catalyst loadings of a few µg per cm^2 electrode surface as well as a <0.5 µm thick binding film of Nafion® makes mass-transport resistances in the electrode structure negligible, with a much easier extraction of kinetic parameters as a result.

3. Experimental

3.1. Investigated carbon materials

13 different carbon samples were examined in this study. Four of these were a series of CBs based on the high-surface-area (770 m^2 g^{-1}) ENSACO®350 G Conductive Carbon Black from

TIMCAL Graphite and Carbon [39]. One of the samples was the as-received material, while three had been heat-treated in inert atmosphere at, respectively, 1800 °C, 2200 °C, and 3000 °C. These four samples are called CB0, CB18, CB22, and CB30, respectively. They were supplied by collaborators at the Technical University of Denmark.

Four other samples were a series of few-walled carbon nanotubes (FWCNTs) synthesized by a procedure described by Rakov et al. [40]. These are CNTs with mainly 2–4 walls, outer tube diameter of 1.8–7.7 nm, inner diameter of 0.6–5.8 nm, and specific surface area of 400 m^2 g^{-1}. Three of the samples were purified in HCl after their synthesis. The sample named FWCNT_1 was not treated any further, while the samples FWCNT_2 and FWCNT_3 were subsequently boiled in a 1:1 mixture of 2 M HNO$_3$ and 1 M H$_2$SO$_4$ for 2 h and 4 h, respectively. The forth sample—FWCNT_4—was purified and activated in one step by boiling in an acid mixture identical to the above-mentioned for 6 h. These samples were prepared and supplied by partners at Helsinki University of Technology (now Aalto University, School of Science).

Graphitized multi-walled carbon nanotubes (GMWCNTs) were purchased from Timesnano. They were three different versions of Timestub^{TM} GMWCNTs, which have lengths of about 50 μm, outer and inner diameters of 8–15 nm and 3–5 nm, respectively, surface area > 117 m^2 g^{-1}, and high electrical conductivity of > 100 S cm^{-1} [41]. One of these commercial samples had not been subjected to any surface-functionalization treatment, one was functionalized by 1.85 wt% hydroxyl groups, and one was functionalized by 1.20 wt% carboxyl groups. These samples are referred to as GMWCNT, GMWCNT–OH, and GMWCNT–COOH, respectively. The purity of the products was stated to be in excess of 99.9 wt% [41].

One CNF sample (SD-CNF) was also included in the study. This was Vapor Grown Carbon Fibre^{TM} from Showa Denko K.K, which is a highly crystalline, graphitized material consisting of tubular fibres with lengths of 10–20 μm, diameter of 0.15 μm, and wall thickness of 40 nm. The surface area of the product is 13 m^2 g^{-1} and it has a low electrical resistance of 0.012 Ω cm [42].

Finally, VULCAN® XC72 from Cabot Corporation was included in the XPS and RRDE tests as a reference, since it is a very widely used conductive CB for catalyst support in PEMFC electrodes. It exhibits excellent conductivity, high purity, ease of dispersion, and it has a particle size around 30 nm and a surface area of about 230–240 m^2 g^{-1} [4,43,44]. It is referred to as Vulcan in the present work.

3.2. Electron spin resonance (ESR) spectroscopy

Samples for ESR analysis were prepared by mixing the carbon material with MgO. The MgO used was chemical grade MgO, which had been annealed at 1000 °C for 10 h in air since this was found to improve its properties as an ESR reference. The optimal carbon concentration for the ESR analysis was found to be 10 wt%. This composition was obtained by mixing 2.0 mg of carbon powder and 18.0 mg of annealed MgO, which was ground in a mortar to obtain a macroscopically homogeneous mixture. 1 mg of this mixture was transferred to a 5-mm ESR quartz tube, which was sealed by a plastic cap and placed in the cavity of the ESR spectrometer.

ESR spectra in a 400-G B range comprising the appearing signals about a g value of 2.0 were recorded at room temperature with a BRUKER EMP-A/A/P system. Microwave radiation with a fixed frequency in the range of 9.42–9.86 GHz was used. Data was acquired as first derivatives of absorption, and 10 scans recorded with a step size of 0.4 or 0.5 G were accumulated for each spectrum. The software used for spectrometer control, data acquisition, and spectral analysis was BRUKER Xenon 1.1b.22.

Spectra were recorded of the four samples CB0–CB30, the four FWCNT samples, the three GMWCNT samples, the SD-CNF sample,

and pure annealed MgO (1 mg). g values were calculated according to Eq. (1) from resonance field strengths extracted from the recorded spectra. As basis for this calculation of g the B value at the local minimum of the derivative of the recorded spectrum was used. The signals were assigned to MgO, localized spins in carbon, and conduction electrons in carbon, respectively, based on their g values. Signal intensities were obtained from double-integration of the recorded spectra. For all samples the integration interval used to obtain the intensity of the carbon signal was the resonance B value ± 100 G; hence also embracing the relatively small MgO signal. The integration interval applied for quantifying the MgO reference peak had to be adjusted to the actual peak width which varied slightly with sample type and experimental conditions. Hence it was the resonance B ± 5.1 G for most CB samples, ±7.0 G for all GMWCNT samples, ±8.7 G for all FWCNT samples, and ±6.5 G for SD-CNF. The intensity of the carbon signal was corrected for the total contribution from the MgO, which was calculated from the intensity of the MgO reference peak in the spectrum in question. The corrected carbon intensity was then divided by the intensity of the reference peak to yield the relative signal intensity.

3.3. X-ray photoelectron spectroscopy (XPS)

The carbon samples for XPS analysis were prepared by spreading a few milligrams of the carbon powder on a circa 1 cm^2 piece of adhesive aluminium foil by the use of a cotton stick. The foil was then attached to a similar-size piece of metal sheet, which was mounted on the sample holder and introduced into the vacuum chamber.

All XPS analyses were conducted in ultrahigh vacuum (10^{-10}–10^{-8} mbar). The X-ray source was a magnesium anode emitting Mg K_α photons with energy of 1253.6 eV. XPS spectra of Vulcan and the four samples CB0–CB30 were recorded in a PHI electron spectrometer, while spectra of the four FWCNT and three GMWCNT samples and SD-CNF were recorded using a Specs electron spectrometer. The PHI electron spectrometer is a Φ 25–270 AR Precision Electron Energy Analyser W/R in a Perkin-Elmer PHI Model 560 ESCA/SAM set-up, while the latter equipment is largely homebuilt from Specs components.

With the PHI spectrometer overview spectra were produced by averaging five scans performed in the broad detection range of 400–1260 eV (kinetic energy) using a step size of 0.5 eV and a pass energy of 50 eV. Detailed spectra of the region encompassing the C 1s peak were obtained by averaging ten scans in the range 900–1000 eV with step size of 0.1 eV and pass energy of 25 eV. For all measurements with this equipment the count time was 0.5 s, the applied X-ray power 250 W, the multiplier voltage 7.0 kV, and the X-ray voltage 1500 V.

For overview spectra on the Specs set-up—which yields a better signal sensitivity than the PHI—three scans in the range 400–1260 eV were used for the FWCNT samples, while one scan in the range 200–1260 eV were used for the GMWCNT and SD-CNF samples. The step size and pass energy were 0.5 eV and 80 eV, respectively, for the overview spectra. C 1s detail spectra at 900–1000 eV were composed of five scans for the FWCNT samples and three scans for the GMWCNT and SD-CNF samples, conducted with steps of 0.1 eV and pass energy of 40 eV. Detail spectra at the O 1s signal were recorded of the GMWCNT and SD-CNF samples by three scans at 670–740 eV, 0.1-eV steps, and 40-eV pass energy. The count time was 0.5 s, the applied X-ray power was 125 W, and the detector and bias voltages were 2600 V and 90 V, respectively, for all measurements on the Specs spectrometer.

Data processing was performed by the use of the software CasaXPS. The measured kinetic energy was converted to electron binding energy, and if needed the spectra were slightly shifted in order for the peak representing the C 1s electrons to assume a value

of about 284.6 eV—most pronounced shifting (up to 13 eV) was required for the spectra recorded with the PHI spectrometer due to instrumental conditions. Integration in the peak regions was performed using linear backgrounds in ranges of approximately 21 eV, 13 eV, and 10 eV for the C 1s, O 1s, and F 1s peaks, respectively. The atomic composition of a sample was calculated from the areas of the signals in the overview spectrum by the use of appropriate instrument-specific sensitivity factors.

3.4. Thin-film rotating ring–disc electrode (RRDE) measurements

All carbon samples for the electrochemical measurements were initially subjected to a mild heat treatment in oxidizing and reducing atmospheres in order to remove impurities. This was done in a tube furnace at 300 °C in a stream of 10% O_2/Ar for 30 min followed by a stream of 50% H_2/Ar for another 30 min.

For the preparation of thin-film electrodes of the various carbon materials, suspensions containing 140 µg mL^{-1} carbon were made. Ultrapure water (18.2 MΩ) was used for the suspensions of Vulcan and the four samples CB0–CB30, while a mixture of 20 wt% isopropanol (≧99.8%, Sigma–Aldrich CHROMASOLV®) and 80 wt% ultrapure water was used for the suspensions of the FWCNT samples, the GMWCNT samples, and the sample of SD-CNF. Ultrasonication for 1–2 h as needed was applied. In some cases slight improvement of the isopropanol-containing suspensions could be obtained by increasing the isopropanol concentration, but 20 wt% was found to be the practical upper limit as the following drop-coating electrode manufacturing was made very difficult by the lower polarity of suspensions containing more isopropanol. The use of other dispersion-facilitating agents than the highly volatile isopropanol was purposely avoided in order to exclude any other possible electrochemical responses than those related to the intrinsic properties of the carbon materials.

An interchangeable ring–disc electrode assembly from Pine Research Instrumentation Inc. consisting of a mirror-polished glassy-carbon (GC) disc insert (AFED050P040GC) and a Pt-ring tip (AFE6R1PT) was applied. 15.0 µL suspension was carefully spread on the disc, so that the drop covered the entire 5.0-mm diameter disc surface while yet being fully confined to the disc. The RRDE assembly was left for 45–75 min for the solvent to evaporate in a stream of Ar in a custom-built chamber. The resulting loading was 11 µg carbon per cm^2 of GC-disc surface. Relatively homogeneous coverings were obtained for Vulcan and CB0, while a certain extent of agglomeration was observed for most of the other materials, resulting in varying qualities of dispersion on the disc. Since mass transport is not a critical factor in the processes involved in the RRDE experiments on the carbon material, the less-than-perfect homogeneities of the electrodes were accepted. 15.0 µL of a 0.027 wt% aqueous Nafion® (10 wt.% dispersion in water, EW 1100, Aldrich) solution was then spread on top of the dried porous carbon layer on the disc. Again the solvent was evaporated in Ar stream (45–75 min), after which the RRDE assembly was mounted in the electrochemical setup and immersed into the electrolyte for measurements.

The RRDE setup was based on equipment from Pine Research Instrumentation including an AFCBP1E bipotentiostat. After Math software was used to control the bipotentiostat as well as for the data acquisition. The volume of the electrochemical cell was circa 200 mL and the electrolyte was 0.5 M $HClO_4$ (70%, Fluka *Trace*SELECT®) in ultrapure water. Pt wire in an electrolyte-filled fine-fritted glass tube was used as counter electrode, and a dynamic hydrogen electrode (DHE) with a potential on the order of −16 mV vs. the reversible hydrogen electrode (RHE) [45] was used as reference electrode.

Prior to the measurements the $HClO_4$ electrolyte was purged by Ar (technical grade, Air Liquide) for about 1 h. The RRDE
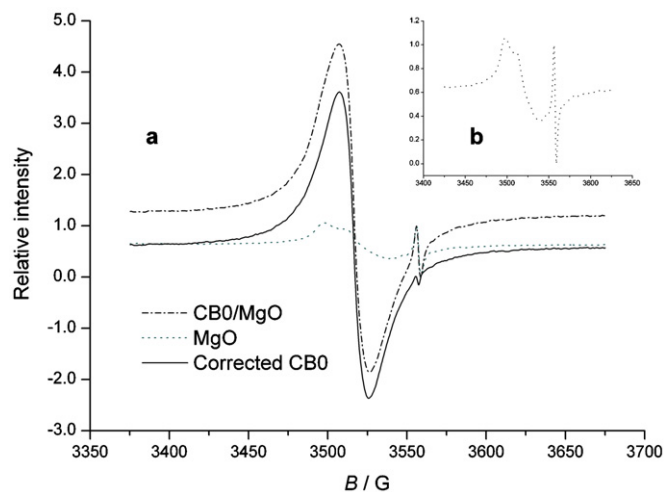

Fig. 1. (a) ESR spectra of un-heat-treated carbon black (CB0) with 90 wt% MgO and pure MgO, and the resulting difference spectrum. (b) Magnification of the MgO signal. CB0 spectrum horizontally shifted − 1.6 G. Intensities normalized by the height of the peak at 3557.4 G in the MgO spectrum.

assembly with the newly prepared electrode was then immersed, and 22 voltammetric cycles between 0 and 1.3 V vs. DHE were performed at a scan rate of 100 mV s^{-1} and a rotation rate of 300 rpm in order to clean the disc electrode. The potential of the Pt ring was held at 1.2 V vs. DHE during the cleaning and fixed at this potential and between all measurements, while the disc was maintained at 0.1 V between measurements. After the electrochemical cleaning five dual-electrode cyclic voltammograms (DECVs) were recorded with the disc potential cycling between 0.066 and 1.0 V at 100 mV s^{-1} and at 300 rpm rotation. This was followed by five DECVs at 0–1.0 V, 20 mV s^{-1}, and 1500 rpm. The electrolyte was then purged by O_2 (N48, Air Liquide) for about 1 h, and the latter DECV procedure (0–1.0 V, 20 mV s^{-1}, 1500 rpm) was repeated under these conditions of O_2-saturation.

The last of the five voltammograms recorded at 100 mV s^{-1} and 300 rpm in Ar-purged electrolyte was exported to Origin®Pro 8.0 and smoothed by the use of appropriate fast-Fourier-transform (FFT) procedures, which was necessary for all recorded data due to noise. The currents related to the ORR were obtained by subtraction of the last DECV at 20 mV s^{-1} and 1500 rpm recorded in Ar-purged electrolyte from the last DECV at 20 mV s^{-1} and 1500 rpm recorded in O_2-purged electrolyte. The fraction of peroxide generated at all potentials was obtained by applying Eq. (2) to the Ar-subtracted curves for the disc and ring currents, respectively. For this calculation a collection efficiency, N, of 0.25, which has been determined previously [15] for the applied RRDE, was used.

4. Results and discussion

4.1. Structure and surface composition

Fig. 1 shows the ESR spectrum of a CB0/MgO sample together with one of pure annealed MgO. The CB0/MgO sample gives rise to an intense signal at an applied magnetic field around 3518 G, which is much less pronounced for the MgO sample (Fig. 1a). For MgO the signal at this field strength is a relatively broad, multi-component feature, while a much sharper, isotropic singlet appears at 3557.4 G (Fig. 1b). The g value of the sharp MgO singlet was found throughout the experiments to be 1.97914 ± 0.00002. It is likely to originate from unpaired electrons in stable radicals associated with lattice defects [46,47]. Since it is a distinct peak well-resoluble from the other spectral features for MgO and from those for carbon, it is well-suited as reference signal and is therefore used as such in this
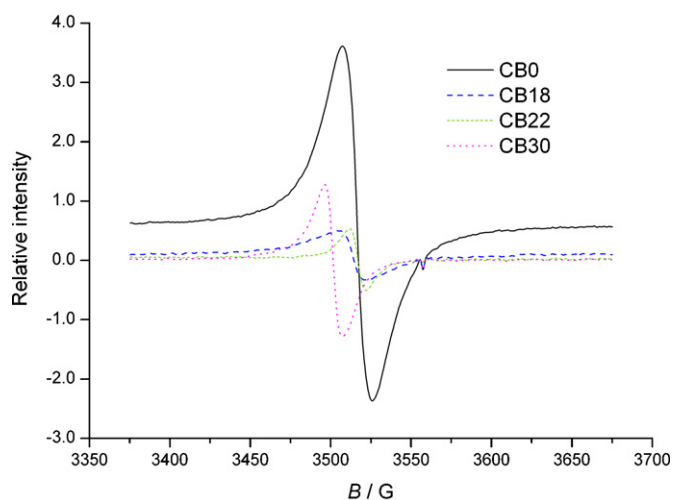
Fig. 2. ESR spectra of un-heat-treated carbon black (CB0) and carbon black heat-treated at 1800 °C (CB18), 2200 °C (CB22), and 3000 °C (CB30), respectively. Field- and intensity-normalized to reference peak in spectrum of MgO. MgO spectrum subtracted.

Table 1
Resonance field values (g) and relative signal intensities for un-heat-treated carbon black (CB0) and carbon black heat-treated at 1800 °C (CB18), 2200 °C (CB22), and 3000 °C (CB30), respectively. Uncertainties given as standard errors.

Sample	g value	Relative signal intensity
CB0	2.00191 ± 0.00004	731.8 ± 4.3
CB18	2.00273 ± 0.00013	159.0 ± 3.8
CB22	2.00174^a NA	6.1 ± 18.1
CB30	2.01032 ± 0.00014	125.8 ± 5.5

[a] Irreproducible.

work. Its g value has been found to be constant with time (several months) and temperature (105–300 K), and its intensity relative to that of the broad feature in the spectrum of MgO appears to be stable over time. Furthermore, the intensity of the broad feature in the MgO spectrum is low compared to that of the signal(s) arising from carbon in the same field region. These properties add to the suitability of annealed MgO as internal-reference substance in the quantitative analysis of electronic spin in carbon samples.

In Fig. 1 the intensities in the spectra have been normalized to the height of the reference peak at 3557.4 G in the MgO spectrum. Furthermore, the shown spectrum of CB0 in Fig. 1a has been shifted by 1.6 G towards lower field in order for the reference peak to match that in the MgO spectrum. A difference spectrum resulting from the subtraction of the MgO spectrum from the shifted CB0 spectrum is also included. The subtraction removes the contribution from the MgO almost completely; only a tiny feature is left from the reference peak. The signal in the difference spectrum of CB0 is seen to be an apparent singlet, but it is broad and asymmetric, so it is probably a collection of several individual signals, which indicates that multiple spin-active species are present [48]. Based on its g value (2.002) the signal may be assigned mainly to localized spins. These arise from stable paramagnetic species in the form of odd-alternate neutral free radicals [26] and possibly various surface groups. Such species are present at edges and defects in the (turbostratic) graphitic structure and in the amorphous domains [4].

Normalized difference ESR spectra of the three heat-treated CB samples together with that of the CB0 sample are presented in Fig. 2. For this representation the spectra have been field-normalized to the B value of the centre of the MgO reference peak, which corresponds to a horizontal shift on the order of a few gauss at most. A clear difference between the spectra of the un-heated CB0 sample and the highly graphitized CB30 is observed. Compared to CB0 the resonance field of CB30 is markedly decreased. While the CB0 signal can be assigned mainly to localized spins, that of CB30 ($g = 2.010$) is primarily a result of conduction electrons giving rise to unpaired spins [26]. Results from ESR analyses at lower temperatures (105–170 K; not shown) support this assignment, since the intensity of the CB0 signal decreases drastically with temperature while that of the CB30 signal remains fairly constant. This is indicative of Curie-like and Pauli temperature dependences of the paramagnetic susceptibility which are characteristic for localized

and conduction electrons, respectively [27,49]. In addition, these analyses indicated that a conduction-electron component was also present in the CB0 spectrum.

The signals for CB18 and CB22 are seen from Fig. 2 to be centred at a field close to that of CB0, indicating that the nature of the spin species is similar. However, the intensities of the CB18 and CB22 signals are substantially smaller. In fact, CB22 in most cases showed no intensity at all, and the spectrum shown in the figure may therefore not be representative for this sample. The decreased intensities means that the concentrations of the localized spin species are thus much lower in these intermediately heat-treated samples than in the pristine material. This is due to improved perfection of the crystal structure resulting from facilitated atomic surface diffusion and rearrangement of carbon during the heat treatment [4].

The g values (for the signals in the original spectra) and signal intensities relative to the internal reference signal are given in Table 1 for the CB series. The decreasing trend of the signal intensity with increasing heat-treatment temperature is evident from the numbers in the table. The signal intensity reaches a minimum of close to zero at 2200 °C, and at 3000 °C the intensity has increased somewhat. This agrees well with the results obtained by Castle and Wobschall [48] who found a significant decrease in spin concentration for CBs in the interval of heat-treatment temperature from 1400 °C to 2700 °C and then a slight increase from 2700 °C to 3000 °C. This is explained by a decrease in the number of broken bonds (localized spins) as the number of edge sites and defects is reduced at a rate increasing with temperature. At a sufficiently high temperature the crystallites have become so close to perfect that the concentration of conduction electrons is significant, which gives rise to ESR activity similar to that of polycrystalline graphite. Indeed, XRD results have shown that the distance between the graphene layers (d spacing) decreases from 0.3628 nm in CB0 to 0.3368 nm in CB30—which is close to that of 0.3354 nm in graphite—while the thickness of the crystals increases from 2 to 12.2 nm [13,15].

The increasing perfection of the crystal structure is also evidenced by the g value of the resonance signal. Whereas the g value for the un-heat-treated CB0 of 2.00191 is very close to the free-electron g value of 2.0023, it increases with heat-treatment temperature up to 2.01032 for CB30 (Table 1). This is in agreement with several earlier studies [48,50]. The g value for raw CBs near the free-electron value is attributed to a predominance of localized spins associated with defects and edges, while the high g value for high-temperature-treated CBs is assigned to conduction carriers in large graphitic crystallites. This latter phenomenon is due to enhanced crystallite interlayer interactions (energy band overlap) as a result of increased crystallite size and decreased interlayer distance [50]. The largest possible g value for graphitized CB has been proposed by Arnold [50] to be 2.0182, which should be obtained in the case of a perfectly random arrangement of large graphitic microcrystals. One reason why the highest observed g value in this study (2.01032) is somewhat lower than this maximum is that the growth of the crystallites is impeded by the physical dimensions of the CB particles ($D \approx 26$ nm for CB0), which in this case are too small to allow large enough microcrystals to form.
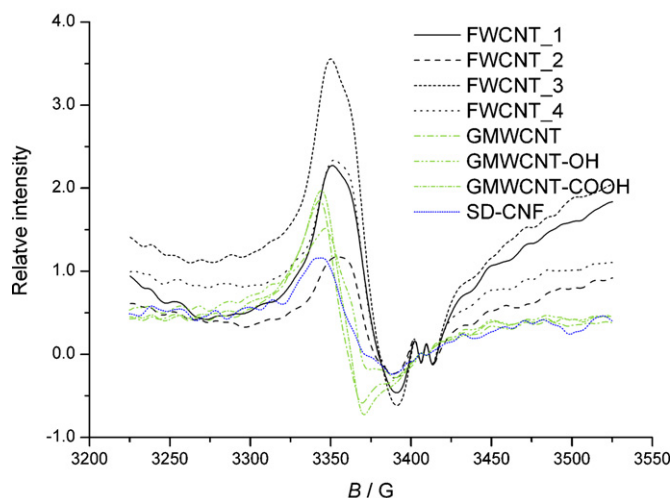
Fig. 3. ESR spectra of the different samples of few-walled carbon nanotubes (FWCNT), graphitized multi-walled carbon nanotubes (GMWCNT), and Showa Denko carbon nanofibre (SD-CNF). Field- and intensity-normalized to reference peak in spectrum of MgO. MgO spectrum subtracted.

Table 2
Resonance field values (g) and relative signal intensities for the samples of few-walled carbon nanotubes (FWCNT), graphitized multi-walled carbon nanotubes (GMWCNT), and Showa Denko carbon nanofibre (SD-CNF).

Sample	g value	Relative signal intensity
FWCNT_1	2.00075	82.0
FWCNT_2	2.00086	9.0
FWCNT_3	2.00086	124.6
FWCNT_4	2.00070	71.4
GMWCNT	2.01204	104.9
GMWCNT–OH	2.00168	140.5
GMWCNT–COOH	2.00425	183.3
SD-CNF	2.00214	108.9

Spectra of the investigated FWCNT, GMWCNT, and SD-CNF samples are shown in Fig. 3. Note that the resonance field strengths are different from those of the previous figures due to a difference in the applied microwave-radiation frequency. However, the g value is independent of this (cf. Eq. (1)). The signals for the FWCNTs are evidently composed of more than one component. There is likely to be contribution from conduction electrons in the low-field end of the signal and from localized electrons in its high-field end. For the GMWCNTs a more singlet-like signal at lower field is observed, which agrees well with other studies [51,52] of multi-walled (MW) CNTs, in which it is concluded that the signal originates from conduction electrons and that the spectrum contains several features similar to those of graphite. Only in the presence of impurities of other carbon allotropes [51] or high concentration of defects [53] would a signal characteristic of localized spin species be observed. For purified single-walled (SW) CNTs only a signal assigned to localized spins has been reported [54]. The intensity of this signal was reported to increase upon shortening of the tubes, in accordance with the expected consequence of increased concentration of edge sites. Based on all this information combined, it is rationalized that the FWCNTs—which are expected to have properties intermediate between those of SWCNTs and MWCNTs—have a significant content of localized electrons due to the relatively high surface area, as well as a pronounced content of conduction electrons. However, the possibility of contamination cannot be excluded.

For the GMWCNTs with their relatively small surface area and good electronic conduction in between the graphene layers it is not surprising that mainly a signal characteristic of conduction electrons is observed. The signal shape for the GMWCNTs seems to have a Dysonian character, in agreement with an observation by Tanaka et al. [55] for MWCNTs. The influence of the surface groups in the two functionalized GMWCNT samples does not appear to be very large. However, for GMWCNT–OH a shoulder in the high-field end of the signal is present which could be related to the presence of the hydroxyl groups. For the FWCNTs an obvious correlation between the appearance of the ESR spectra and the pre-treatment of the samples does not seem to exist. The signals for the un-oxidized FWCNT_1 and the 6-h one-step-treated FWCNT_4 are almost identical, while that of the 2-h-treated FWCNT_2 is a lot smaller and that of the 4-h-treated FWCNT_3 is larger. The conduction-electron component seems to be pronounced in FWCNT_1, FWCNT_3, and FWCNT_4, but less so in FWCNT_2, which is difficult to explain. In the tubular fibres of SD-CNF conduction electrons seem to be dominant. This is consistent with its claimed small *d* spacing of 0.339 nm and high electrical conductivity [42].

The calculated g values and relative signal intensities for the CNT and CNF samples are shown in Table 2. Note that in order to avoid corruption introduced in the correction procedure the g values in Table 2 are obtained from the minimum derivative in the spectra before the subtraction of the reference spectrum, and they may therefore differ somewhat from what would be expected from the appearance of the signals in Fig. 3. The signals are complex and the single g value assigned for each of them can only be used for a rough estimation of their nature. However, it is clear that the conduction-electron component at lower field (large g) is dominant in the GMWCNT and SD-CNF samples, whereas an additional localized-spin component at higher field (small g) is pronounced in the FWCNT samples. g values of 2.012 (conduction electrons) [51,52] and 2.00 (localized spins) [54] have been reported from other studies on MWCNTs and SWCNTs, respectively.

The overview XPS spectra of the 13 investigated samples are shown in Fig. 4. The spectra of Vulcan and the four CB samples, which were recorded on the PHI spectrometer under different instrumental and slightly different experimental conditions from those used for the other spectra, were magnified to facilitate the comparison. Not surprisingly the spectra show that carbon is the predominant surface element in all the samples, as evidenced by the large peak for the 1s electrons in this element. All the samples also contain some oxygen. For the three GMWCNT samples and
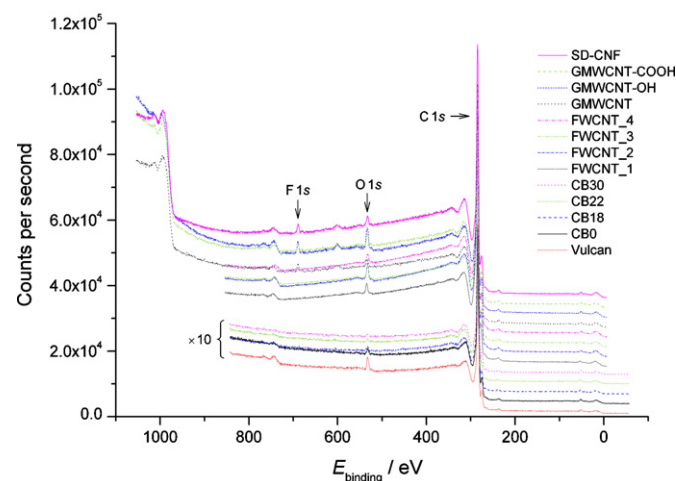

Fig. 4. Overview XPS spectra of the VULCAN® XC72 reference, the four carbon-black (CB) samples, the four few-walled carbon nanotube (FWCNT) samples, the three graphitized multi-walled carbon nanotube (GMWCNT) samples, and Showa Denko carbon nanofibre (SD-CNF). Spectra of Vulcan and CB0–CB30 horizontally shifted by −11 eV and their intensities multiplied by 10 to correct for instrumental and experimental differences. Vertical offset of 3000 counts per second between each spectrum.

Table 3
Surface elemental compositions obtained from the C 1s, O 1s, and F 1s peaks in the overview spectra of the VULCAN® XC72 reference, the four carbon-black (CB) samples, the four few-walled carbon nanotube (FWCNT) samples, the three graphitized multi-walled carbon nanotube (GMWCNT) samples, and Showa Denko carbon nanofibre (SD-CNF).

Sample	Carbon concentration (at%)	Oxygen concentration (at%)	Fluorine concentration (at%)
Vulcan	97.3	2.7	–
CB0	99.0	1.0	–
CB18	99.0	1.0	–
CB22	99.4	0.6	–
CB30	99.5	0.5	–
FWCNT_1	98.5	1.5	–
FWCNT_2	98.1	1.9	–
FWCNT_3	98.2	1.8	–
FWCNT_4	98.9	1.1	–
GMWCNT	98.4	1.1	0.5
GMWCNT–OH	95.1	3.9	1.0
GMWCNT–COOH	97.6	1.8	0.7
SD-CNF	98.2	1.1	0.7

SD-CNF fluorine was detected in addition. Whether this is contamination from the manufacturing process, the storage, or from the vacuum chamber is not known. The surface elemental compositions obtained from the intensities of the C 1s, O 1s, and F 1s peaks are given in Table 3.

All the CBs contain considerably less surface oxygen than the reference Vulcan. It is somehow interesting that the oxygen content is lower in the high-surface-area CB0 than in Vulcan which has a surface area of less than a third of that of CB0. The heat treatment of CB at 1800 °C does not seem to reduce the oxygen content, but at 2200 °C and above it is about halved. It is expected that all oxygen surface groups are decomposed at these temperatures. However, it is very difficult to completely avoid the presence of oxygen during heat treatment [56], and hydroxyl groups appear be stable even at rather high temperatures [4]. Also, some oxygen may chemisorb after the heat treatment when the samples are exposed to the atmosphere. Anyway, the concentration is low in all cases, and it is approaching the detection limit in CB22 and CB30.

The FWCNT_2 and FWCNT_3, which have been purified and boiled in oxidizing acid, have a little higher oxygen content than the only-purified FWCNT_1. However, the treatment time (2 h for FWCNT_2 and 4 h for FWCNT_3) does not seem to affect the oxygen concentration. The 6-h one-step-treated FWCNT_4 contains less oxygen than the other samples, which indicates that the HCl purification step is important for the introduction of oxygen functionalities.

For the GMWCNTs higher oxygen contents are found in the hydroxyl- and carboxyl-functionalized samples, GMWCNT–OH and GMWCNT–COOH, respectively. In both cases the obtained oxygen concentrations of 3.9 at% and 1.8 at%, respectively, are higher than the contents stated by the manufacturer, which are 1.85 wt% OH corresponding to 1.3 at% O and 1.20 wt% COOH corresponding to 0.64 at% O, respectively. These divergences may be due to the presence of other oxygen-containing species or differences between surface and bulk compositions.

Relevant segments of the C 1s detail spectra of all the samples and the O 1s detail spectra of the GMWCNT samples and SD-CNF are presented in Figs. 5 and 6, respectively. The C 1s spectra (Fig. 5) consist of a large signal which tails considerably in its high-energy side. For the CB samples and Vulcan an additional and rather significant component in the low-energy side of the signal is seen. The origin of such a feature is unclear, but it might be related to the experimental conditions since these five samples were examined in the PHI setup where an X-ray power of 250 W was used as opposed to the 125 W used in the Specs setup applied for the analysis of the
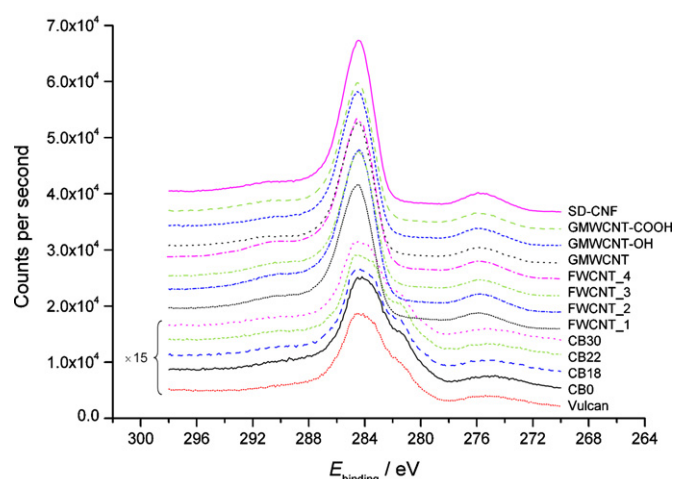

Fig. 5. Detail XPS spectra of the C 1s peak of the VULCAN® XC72 reference, the four carbon-black (CB) samples, the four few-walled carbon nanotube (FWCNT) samples, the three graphitized multi-walled carbon nanotube (GMWCNT) samples, and Showa Denko carbon nanofibre (SD-CNF). Horizontally shifted to have maximum intensity at 284.5 eV, and intensity of Vulcan and CB0–CB30 multiplied by 15 to correct for instrumental and experimental differences. Vertical offset of 3000 counts per second between each spectrum.

other eight samples. This higher power of the incoming radiation may induce adverse effects in the CB material in the form of the formation of new species or states. Whereas this lower-energy feature for the CB material is unexpected, the tailing towards higher energy in all the spectra is expected and is due C–C aliphatic bonds, different C–O and C=O bonds, and π–π^* interactions in addition to the predominant C=C aromatic bonds [34]. Deviations from graphitic (sp^2) nature caused by contamination and chemical modifications give a disordered lattice structure in which the extended π system of the graphitic rings is broken up, and the result is broadening of the C 1s line towards higher binding energy than that of the C 1s electron in graphitic carbon (284.6 eV in graphite) [33,34]. The C 1s signals in the spectra recorded with the Specs spectrometer (i.e., those of the FWCNT, GMWCNT, and SD-CNT samples) were found to have a maximum at 284.5 eV. This corresponds quite well to findings by Chen et al. [57] who found the location of the C 1s peak to be 284.3 eV for MWCNTs and also arrived at the conventional value of 284.6 eV for graphite. The authors ascribed the small negative
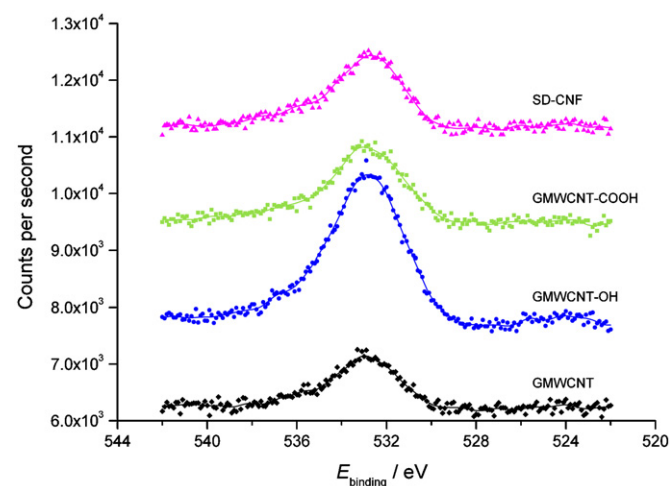

Fig. 6. Detail XPS spectra of the O 1s peak of the three graphitized multi-walled carbon nanotube (GMWCNT) samples and Showa Denko carbon nanofibre (SD-CNF). Individual vertical offset between the spectra. Curves represent 5-point FFT smoothings.
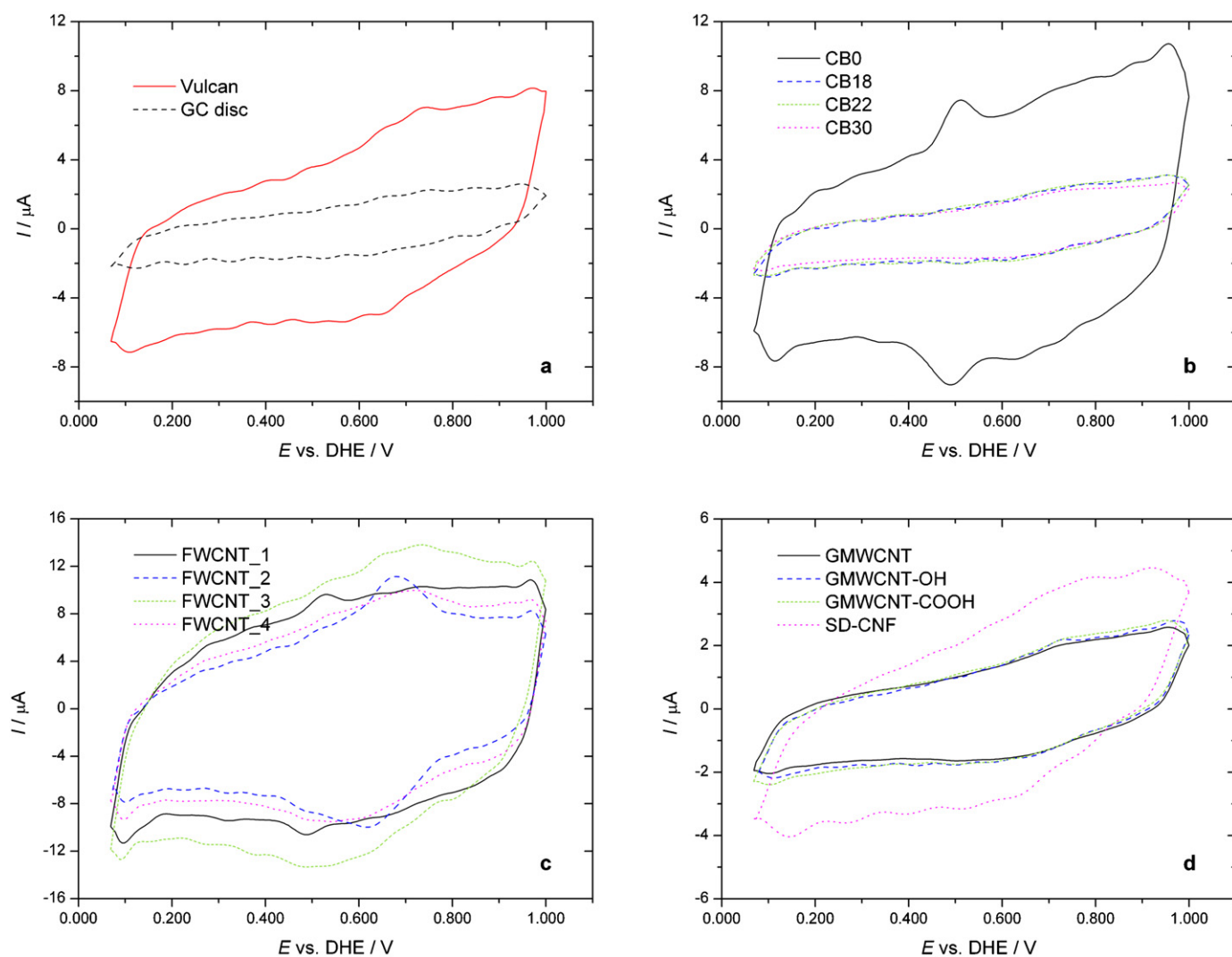
Fig. 7. Cyclic voltammograms in the potential range of 66–1000 mV vs. DHE of (a) the bare glassy-carbon (GC) disc electrode and a thin-film VULCAN® XC72 electrode, (b) thin-film electrodes of the four carbon-black (CB) samples, (c) thin-film electrodes of the four few-walled carbon nanotube (FWCNT) samples, and (d) thin-film electrodes of the three graphitized multi-walled carbon nanotube (GMWCNT) samples and Showa Denko carbon nanofibre (SD-CNF). Carbon loading of 11 μg cm^{-2} for all thin-film electrodes. Ar-purged 0.50 M HClO$_4$ electrolyte, 100 mV s^{-1} scan, 300 rpm rotation.

shift of 0.3 eV for the CNT material to weaker binding between the carbon atoms caused by the curvature of the graphene sheets and the larger interlayer distance.

In the O 1s spectra (Fig. 6) signals peaking at close to 533 eV are seen. The signal is larger for GMWCNT–OH than for the three other samples due to its higher oxygen content (cf. Table 3). Apart from this the spectra do not differ very much. Two main components are expected to be present; namely one around 531–532 eV arising from doubly bonded oxygen and one around 532–533.5 eV stemming from singly bonded oxygen [34,58]. Based on this the oxygen in all samples appear to be mainly singly bonded; even GMWCNT–COOH does not show a significant contribution from C=O.

Further interpretation of the XPS signals was found not to be possible as discussed in detail elsewhere [15]. The explanation involves the low content of oxygen species and the intrinsic asymmetry of the C 1s signal [56,34,59]. Thus unambiguous deconvolution of the C 1s signal into individual components—such as peaks at 286.7 eV and 288.9 eV for C–O bonds and C=O bonds, respectively [60]—could not be carried out. A curve fitting in the C 1s signal should be based on the intensities obtained from the O 1s signal, but since the oxygen-to-carbon ratio is much lower

than the area of the tailing part of C 1s signal relative to the total area of this signal, a meaningful fitting could not be done under the constraint of O/C stoichiometry only. Other parameters would be needed in order to make good and unequivocal interpretations of the spectra in this case. Such parameters could be intensities, line shapes, line widths, and binding energies obtained from reference samples of totally pure and perfect versions of the investigated material [33,56,34], but such samples do not exist.

Cyclic voltammograms (CVs) of all the tested thin-film electrodes in Ar-purged electrolyte are shown in Fig. 7, in which the CVs of the bare GC disc and that of a thin-film electrode of the Vulcan reference is also included. The currents in the CVs of the carbon materials are mainly ascribed to double-layer capacitance [4,6]; however, the CVs are a bit skewed, which is probably due to an uncompensated series resistance. The capacitive current of the GC disc is seen to be significantly smaller than that of Vulcan (Fig. 7a), which is due to the smaller real surface area. From a comparison of the current of CB0 (Fig. 7b) with that of Vulcan it is seen than the former is not very much bigger than the latter, although the specific surface area of CB0 is about three times as large as that of Vulcan (770 vs. 230–240 m^2 g^{-1}). The capacitance is of course expected to increase with the surface area, but for the

high-surface-area CB0 a considerable part of the surface is found in micropores, where it may not be accessible to the electrolyte. Also, the content of oxygen is higher (about three times) in Vulcan than in CB0 (cf. Table 3), and since surface oxide groups may contribute to the double-layer capacitance and improve the wettability of the carbon surface, this may account for some of the relatively high capacitance of Vulcan compared to CB0 [4]. Heat treatment is seen to decrease the capacitance of the CB significantly (Fig. 7b), which can be attributed to decreases in surface area, content of oxygen groups, and defect concentration [4,6]. For the heat-treated samples the double-layer capacity is almost identical to that of the GC disc.

The currents for the FWCNT samples (Fig. 7c) are the largest observed for all the samples (note the different scales in Fig. 7). This correlates well with their relatively high surface area (400 $m^2 g^{-1}$). FWCNT_3 shows the highest current, which could be indicative of a higher concentration of defects being introduced by the activation process performed on this sample (boiling in HNO_3/H_2SO_4 for 4 h) than by the processes used for the other FWCNT samples. This interpretation would be in accordance with the ESR findings (Fig. 3 and Table 2). The GMWCNT samples (>117 $m^2 g^{-1}$) have small capacitances (Fig. 7d) close to that of the bare GC disc. They are similar among the three samples, although the oxygen contents are higher in GMWCNT–OH and GMWCNT–COOH than in the
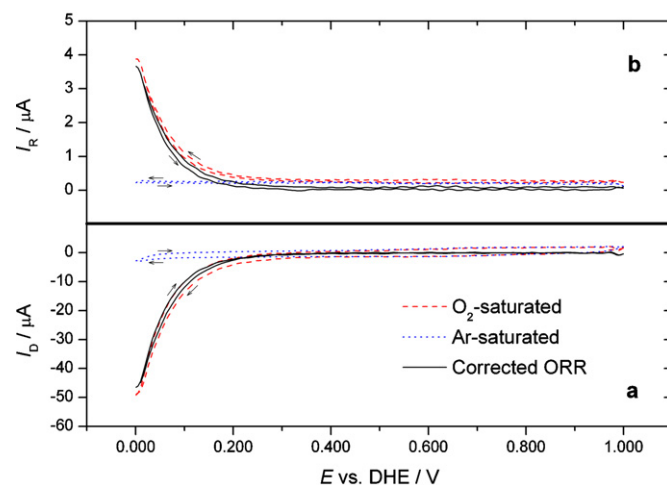

Fig. 8. Cyclic voltammograms in the potential range of 0–1000 mV vs. DHE (a) and the corresponding currents through the ring at 1200 mV (b) of a thin-film VULCAN® XC72 electrode (11 $\mu g\,cm^{-2}$) in O_2-saturated and Ar-saturated electrolyte, respectively, and the corrections obtained by subtraction (O_2–Ar). 0.50 M $HClO_4$ electrolyte, 20 mV s^{-1} scan, 1500 rpm rotation. Sweep direction indicated by arrows.
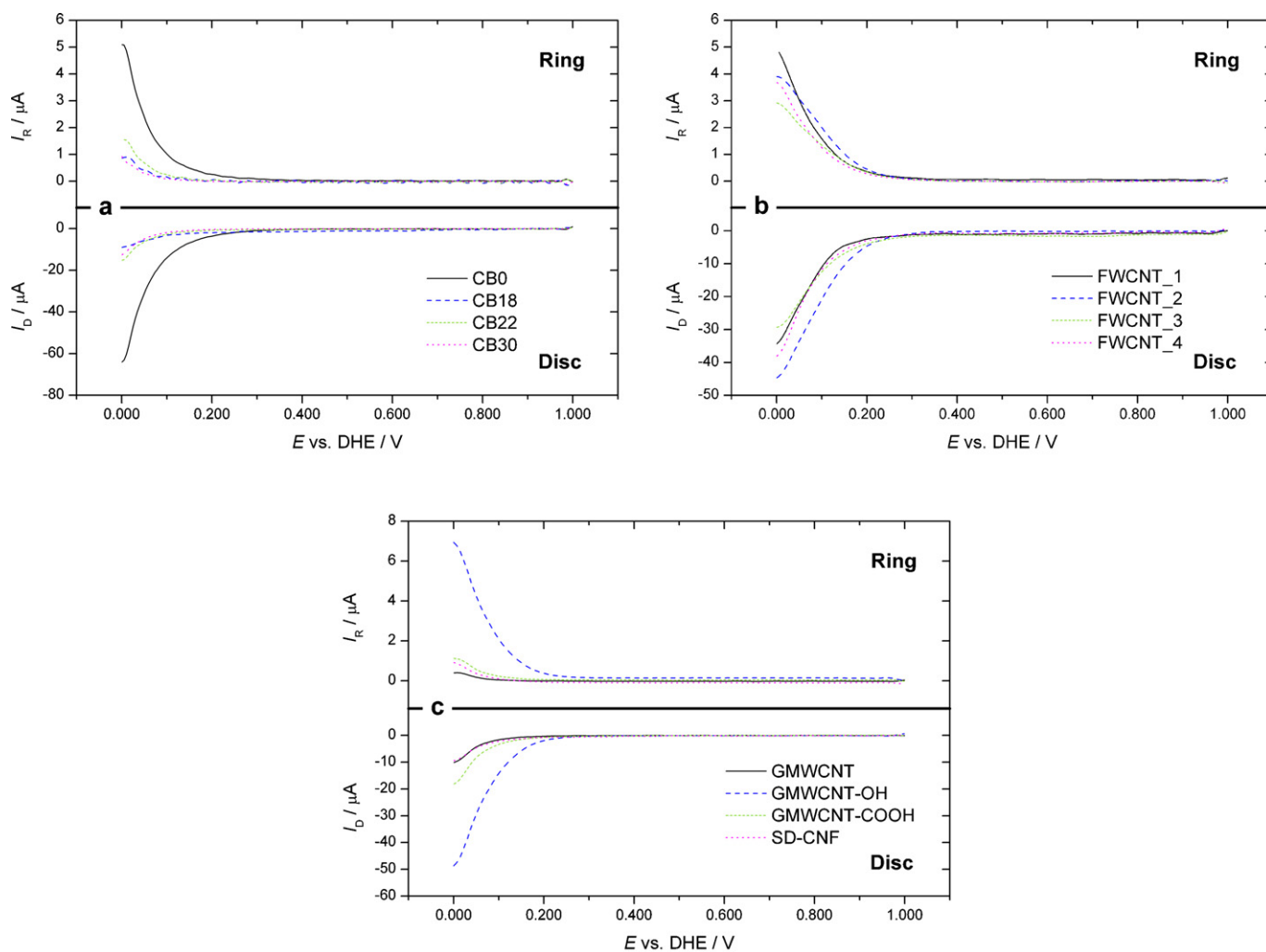

Fig. 9. ORR currents in the potential range of 0–1000 mV vs. DHE and the corresponding currents through the ring at 1200 mV for thin-film electrodes (11 $\mu g\,cm^{-2}$) of (a) the four carbon-black (CB) samples, (b) the four few-walled carbon nanotube (FWCNT) samples, and (c) the three graphitized multi-walled carbon nanotube (GMWCNT) samples and Showa Denko carbon nanofibre (SD-CNF). 0.50 M $HClO_4$ electrolyte, 20 mV s^{-1} scan, 1500 rpm rotation. All positive-going sweeps.
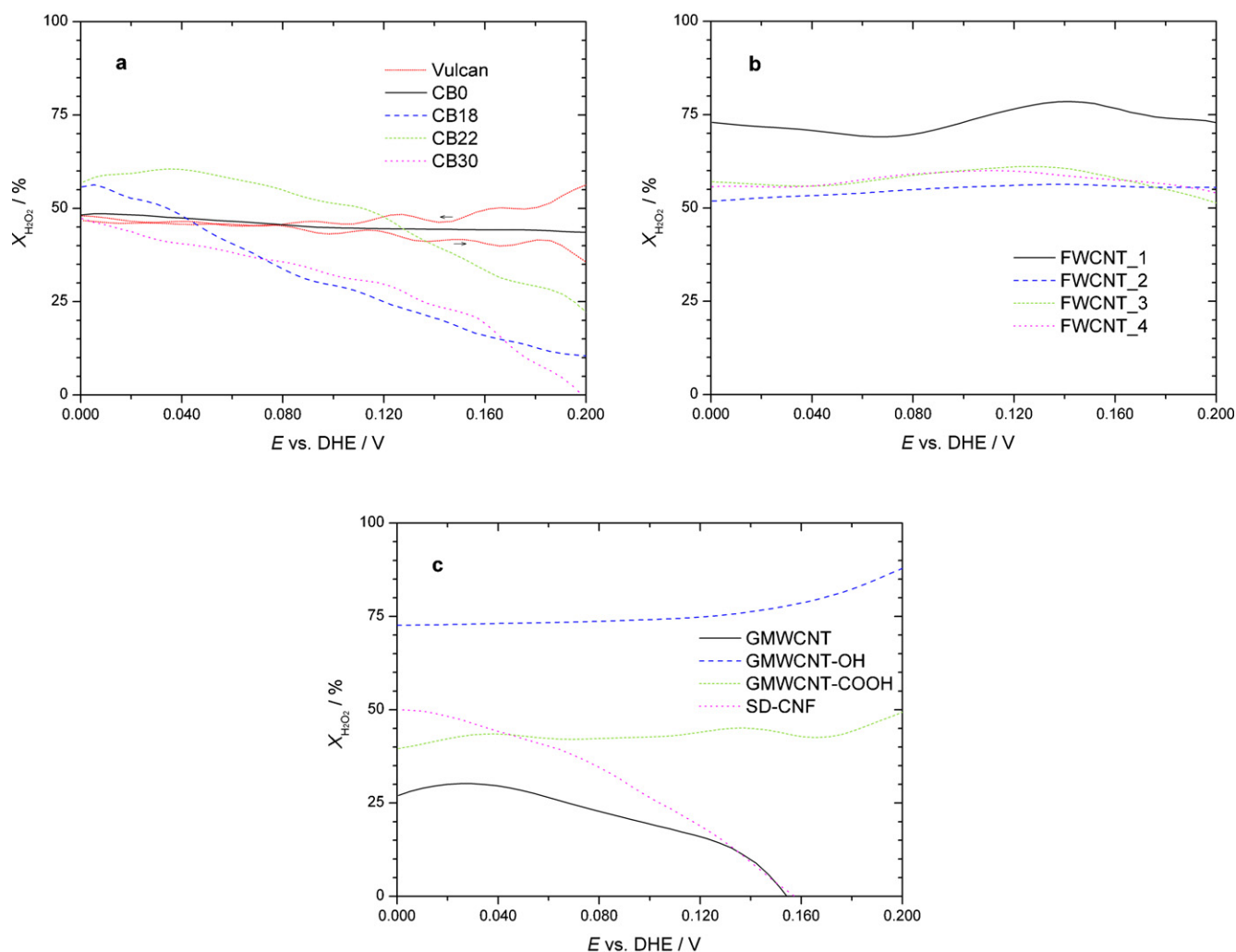
Fig. 10. Percentages of peroxide formed in the range of 0–200 mV vs. DHE on thin-film electrodes (11 μg cm^{-2}) of (a) VULCAN® XC72 and the four carbon-black (CB) samples, (b) the four few-walled carbon nanotube (FWCNT) samples, and (c) the three graphitized multi-walled carbon nanotube (GMWCNT) samples and Showa Denko carbon nanofibre (SD-CNF). 0.50 M HClO$_4$ electrolyte, 20 mV s^{-1} scan, 1500 rpm rotation. Positive-going sweeps for all samples; negative-going sweep included for Vulcan (sweep direction indicated by arrows).

un-functionalized GMWCNT. The SD-CNF shows a slightly higher capacitance than the GMWCNTs. This is somewhat surprising due to its very low surface area (13 m^2 g^{-1}).

The distinct peak around 0.5 V in the CVs of CB0 and FWCNT_1 suggests the presence of quinone functionalities which give rise to Faradaic currents due to hydroquinone–quinone redox interconversion [4,35]. A different electrochemically active species seems to be present in FWCNT_2 which has a peak pair around 0.65 V. This could be quinone-like groups in different environments on the surface. More indistinct features are seen for FWCNT_3 and FWCNT_4, while for the remaining samples not very strong evidences of electroactive groups are present (the tiny waves in many of the curves originate from noise in the experimental data not being fully eliminated by the data smoothing).

4.2. ORR activity and peroxide generation

In Fig. 8 disc and ring currents versus disc potential are depicted for a thin-film electrode of Vulcan in O$_2$-saturated electrolyte as well as in Ar-saturated electrolyte. The difference between the CVs recorded under these two conditions is also shown. The difference curves have been obtained by subtraction of the currents recorded in the absence of O$_2$ (i.e., in Ar-electrolyte) from those recorded in

its presence, and these curves thus represent the currents arisen solely as a consequence of O$_2$ reduction, with the contributions from processes not related to the ORR being excluded. Thus the double-layer capacitance contribution at the disc is nearly eliminated. As a consequence the difference between the positive-going and the negative-going sweeps is not very big, and in the following figures only the currents representing the positive sweeps are shown. For background assessment it was found that the ORR activity of the GC disc was negligible compared to those of the thin-film electrodes of the carbon materials and that the Nafion® layer on top of the electrodes does not affect the recorded currents appreciably [15].

The corrected currents in Fig. 8 are seen to be essentially 0 at potentials above circa 0.2 V. Below, O$_2$ is reduced, which gives rise to a negative current on the disc (Fig. 8a). Vulcan thus shows some ORR activity, but the catalytic effect is indeed very low as evidenced by the very small reduction current and by the huge overpotential on the order of 1 V and which is all in accordance with the low catalytic activity expected for carbon in acid electrolyte [19,22]. The highest disc current of about −50 μA measured at the lower potential limit of 0 V is far from the mass-transport-limited current of −964 μA calculated from the Levich equation for this system [15]. On the ring a positive—but significantly smaller—current is

measured at low potentials (Fig. 8b), which is ascribed to the oxidation of hydrogen peroxide and other oxidizable oxygen species generated on the disc.

The ORR-related currents for the CB, FWCNT, GMWCNT, and SD-CNF samples are shown in Fig. 9. The currents for CB0 are seen to be large compared to those of the heat-treated samples CB18, CB22, and CB30 (Fig. 9a), which must be attributed to the higher surface area and defect concentration of the first-mentioned. These currents are comparable to those of Vulcan (Fig. 8) and the FWCNT samples (Fig. 9b) between which there is not much difference. The currents for GMWCNT–OH are of a similar magnitude and much higher than those of GMWCNT, GMWCNT–COOH, and SD-CNF (Fig. 9c). This marked difference is likely related to the prominent concentration of hydroxyl groups in GMWCNT–OH. This assumption is supported by findings that electrooxidation of the carbon electrodes enhances their activity towards promotion of O_2 reduction ([15], not shown). The electrooxidation is likely to generate reactive surface oxygen species, increase the wettability, and enhance the surface-area by, e.g., opening of blocked micropores [35,61].

The peroxide percentages for all the investigated samples as functions of potential are shown in Fig. 10. They are only depicted up to 0.2 V as the currents running at higher potentials are essentially zero, which thus makes the determination of $X_{H_2O_2}$ from Eq. (2) impossible. Already above 0.1 V fluctuations in the curves are observed, which are due to non-eliminable noise. Generally, for all the examined materials between 25 and 75% of the ORR product at 0 V vs. DHE is seen to be peroxide. On carbon a peroxide pathway of the ORR is known to be favoured, resulting in a substantial share of peroxide product [20–22].

It is seen from Fig. 10a that $X_{H_2O_2}$ for Vulcan is fairly constant at approximately 45 mol% within the depicted potential range. Also, in the lower end of the range there is not much difference between $X_{H_2O_2}$ for the two sweep directions. For CB0 a somewhat similar picture is seen, but the other CB samples show a different behaviour (Fig. 10a), which is a decrease in $X_{H_2O_2}$ with increasing potential. For the FWCNT samples (Fig. 10b) $X_{H_2O_2}$ is nearly constant with potential, and also between the samples; only FWCNT_1 shows a somewhat higher $X_{H_2O_2}$ than the others. On GMWCNT–OH significantly more peroxide is generated than on GMWCNT, GMWCNT–COOH, and SD-CNF (Fig. 10c). The ORR was found to be rather significant on this sample (Fig. 9c), so it seems that the hydroxyl groups promote the ORR, but mainly with peroxide as product. For the un-oxidized, graphitized GMWCNT and SD-CNF, on the contrary, $X_{H_2O_2}$ is seen to rapidly decrease as the potential is raised. This is the same trend as for the heat-treated CB18, CB22, and CB30, so it seems that graphitization lowers the peroxide generation. Defects and hydroxyl groups, on the other hand, may promote peroxide generation.

Overall, it must be kept in mind that the ORR activity of the carbon material is very low compared to that of the noble-metal particles supported on them in high-surface-area fuel-cell catalysts. Some of the peroxide generated on the carbon may also be further electrochemically reduced to water or chemically decomposed on the noble-metal particles [62]. Furthermore, the ORR activity of carbon and hence the peroxide generation only occurs ay potentials below 0.2 V, which is far from the typical range of PEMFC cathode potentials. However, since carbon-supported catalysts are used in both electrodes, the measurable peroxide formation at low potentials may play an important role at the anode where crossover oxygen from the cathode side is almost always present to some extent. At the low potentials present at PEMFC anodes carbon shows its highest ORR activity, and part of the oxygen present here may be reduced by the carbon material to peroxide, which may then promote the degradation of the ionomer and possibly also other components.

5. Conclusion

Structural properties related to electron-spin characteristics and surface oxygen functionalities were investigated for the broad collection of carbon materials. Their electrochemical behaviour in the ORR was examined too, and several interesting connections between this and the structure were found.

For CB it was found that heat treatment at 1800 °C was sufficient to change the electrochemical behaviour as represented by reduced double-layer capacitance, removal of quinone functionality, reduced ORR activity, and somewhat reduced proportion of peroxide generated in the ORR. Higher heat-treatment temperatures did not lead to significant further changes in the electrochemical characteristics. As for the oxygen content, 2200 °C was needed for a decrease to be detected by XPS. This decrease from 1.0 to about 0.6 at% was not followed by further significant decrease upon heat treatment at 3000 °C. ESR analyses showed that the significant concentration of defects in raw CB decreased upon heat treatment up to 2200 °C, but that 3000 °C was necessary in order for conduction electrons to be predominant; i.e., to create pronounced graphitic structure.

FWCNTs showed a relatively high concentration of defects in addition to the expected abundance of conduction electrons. Otherwise the ESR results for the samples of this material were somewhat inconclusive. However, combined with the oxygen contents determined by XPS it may be proposed that purification in HCl prior to acidic oxidation is important for the generation of structural changes necessary for oxygen functionalization. Prolonged time of treatment in HNO_3–H_2SO_4 solution seemed to introduce a higher concentration of structural defects to the purified FWCNT material as evidenced by higher capacitive currents and increased ESR activity, but the oxygen content did not increase. For FWCNT the acidic oxidation was found to reduce the percentage of peroxide product. Electrochemically active surface groups, probably different quinones, were present in the FWCNT samples.

The ESR activity in GMWCNTs is almost exclusively due to conduction electrons; however, a minor contribution from localized spins may reveal the presence of hydroxyl groups in the OH-functionalized version of the material. Surface oxygen contents in the OH-functionalized and COOH-functionalized samples were found to be in twofold excess of those extracted from the specified contents of the respective functional groups. Other oxygen-containing species than those stated by the manufacturer may thus be present. None of these were found to be electrochemically active, but the functional groups present in the OH-functionalized sample seem to have a significant increasing effect on the ORR and the peroxide percentage, which was as high as 75. SD-CNF had mainly graphitic character, low oxygen content, and a rather small electrochemical activity.

Overall, defects and oxygen-containing groups on the surface of the carbons were found to promote the ORR. Especially hydroxyl groups seem to have a significant impact on the ORR, boosting the activity of the carbon material and increasing the percentage of peroxide formed. Defects in/on the carbon material also seem to increase the peroxide generation, and thus graphitization of the carbon lowers the peroxide generation. The type of oxidative pre-treatments of the materials was found to affect all the properties investigated; that is, spin activity, oxygen content, ORR activity, and peroxide generation. Different surface properties as well as structural changes are induced by such pre-treatments.

References

[1] K. Lee, J. Zhang, H. Wang, D.P. Wilkinson, Journal of Applied Electrochemistry 36 (2006) 507–522.
[2] E. Antolini, Applied Catalysis B: Environmental 88 (2009) 1–24.
[3] Y. Shao, G. Yin, J. Zhang, Y. Gao, Electrochimica Acta 51 (2006) 5853–5857.
[4] K. Kinoshita, Carbon Electrochemical and Physicochemical Properties, John Wiley & Sons, Inc., New York, 1988.
[5] J. Wu, X.Z. Yuan, J.J. Martin, H. Wang, J. Zhang, J. Shen, S. Wu, W. Merida, Journal of Power Sources 184 (2008) 104–119.
[6] L.C. Colmenares, A. Wurth, Z. Jusys, R.J. Behm, Journal of Power Sources 190 (2009) 14–24.
[7] H.-S. Oh, J.-G. Oh, S. Haam, K. Arunabha, B. Roh, I. Hwang, H. Kim, Electrochemistry Communications 10 (2008) 1048–1051.
[8] L. Li, Y. Xing, Journal of the Electrochemical Society 153 (2006) A1823–A1828.
[9] L. Li, Y. Xing, Journal of Power Sources 178 (2008) 75–79.
[10] X. Wang, W. Li, Z. Chen, M. Waje, Y. Yan, Journal of Power Sources 158 (2006) 154–159.
[11] E. Yli-Rantala, A. Passanen, P. Kauranen, V. Ruiz, M. Borghei, E. Kauppinen, A. Oyarce, G. Lindbergh, C. Lagergren, M. Darab, S. Sunde, M. Thomassen, S. Ma-Andersen, E. Skou, Fuel Cells 11 (2011) 1–11.
[12] S.M. Andersen, E.M. Skou, Institute of Chemical Engineering, Biotechnology and Environmental Technology, University of Southern Denmark, unpublished results.
[13] L. Qingfeng, Department of Chemistry, Technical University of Denmark, unpublished results.
[14] I. Kvande, S.T. Briskeby, M. Tsypkin, M. Rønning, S. Sunde, R. Tunold, D. Chen, Topics in Catalysis 45 (2007) 81–85.
[15] M.J. Larsen, Investigation of alternative carbon materials for fuel-cell catalyst support, Ph.D. thesis, Institute of Chemical Engineering, Biotechnology and Environmental Technology, University of Southern Denmark, Odense, 2010.
[16] A.B. LaConti, M. Hamdan, R.C. McDonald, Mechanisms of membrane degradation, in: W. Vielstich, A. Lamm, H.A. Gasteiger (Eds.), Handbook of Fuel Cells. Fundamentals, Technology and Applications, vol. 3: Fuel Cell Technology and Applications: Part 1, John Wiley and Sons Ltd, Chichester, 2003, pp. 647–662.
[17] D.E. Curtin, R.D. Lousenberg, T.J. Henry, P.C. Tangeman, M.E. Tisack, Journal of Power Sources 131 (2004) 41–48.
[18] N. Ramaswamy, N. Hakim, S. Mukerjee, Electrochimica Acta 53 (2008) 3279–3295.
[19] E. Yeager, Electrochimica Acta 29 (1984) 1527–1537.
[20] K. Kinoshita, Electrochemical Oxygen Technology, John Wiley & Sons, Inc., New York, 1992.
[21] H.S. Wroblowa, Y.-C. Pan, G. Razumney, Journal of Electroanalytical Chemistry 69 (1976) 195–201.
[22] U.A. Paulus, T.J. Schmidt, H.A. Gasteiger, R.J. Behm, Journal of Electroanalytical Chemistry 495 (2001) 134–145.
[23] M. Inaba, T. Kinumoto, M. Kiriake, R. Umebayashi, A. Tasaka, Z. Ogumi, Electrochimica Acta 51 (2006) 5746–5753.
[24] U.H. Jung, S.U. Jeong, K. Chun, K.T. Park, H.M. Lee, D.W. Choi, S.H. Kim, Journal of Power Sources 170 (2007) 281–285.
[25] V.A. Sethuraman, J.W. Weidner, A.T. Haug, M. Pemberton, L.V. Protsailo, Electrochimica Acta 54 (2009) 5571–5582.
[26] L.S. Singer, I.C. Lewis, Applied Spectroscopy 36 (1982) 52–57.
[27] E.M. Cashell, V.J. McBrierty, Journal of Materials Science 12 (1977) 2011–2020.
[28] K. Wakabayashi, Electronic and magnetic properties of nanographites, in: T.L. Makarova, F. Palacio (Eds.), Carbon-Based Magnetism. An Overview of the Magnetism of Metal Free Carbon-Based Compounds and Materials, Elsevier B.V, Amsterdam, 2006, pp. 279–304.
[29] A.V. Rode, A.G. Christy, E.G. Gamaly, S.T. Hyde, B. luther-Davies, Magnetic properties of novel carbon allotropes, in: T.L. Makarova, F. Palacio (Eds.), Carbon-Based Magnetism. An Overview of the Magnetism of Metal Free Carbon-Based Compounds and Materials, Elsevier B.V, Amsterdam, 2006, pp. 463–482.
[30] R.V. Parish, NMR, NQR, EPR, and Mössbauer Spectroscopy in Inorganic Chemistry, Ellis Horwood Limited, Chichester, 1990.
[31] M.J. Larsen, Y. Ma, H. Qian, H. Toftlund, P.B. Lund, E.M. Skou, Solid State Ionics 181 (2010) 201–205.
[32] C.S. Fadley, Basic concepts of X-ray photoelectron spectroscopy, in: C.R. Brundle, A.D. Baker (Eds.), Electron Spectroscopy: Theory, Techniques and Applications, vol. 2, Academic Press Inc., New York, 1978, pp. 1–156.
[33] T. Takahaga, A. Ishitani, Carbon 22 (1984) 43–46.
[34] E. Desimoni, G.I. Casella, A. Morone, A.M. Salvi, Surface and Interface Analysis 15 (1990) 627–634.
[35] K.H. Kangasniemi, D.A. Condit, T.D. Jarvi, Journal of the Electrochemical Society 151 (2004) E125–E132.
[36] W.J. Albery, M.L. Hitchman, Ring-Disc Electrodes, Oxford University Press, London, 1971.
[37] D. Pletcher, R. Greef, R. Peat, L.M. Peter, J. Robinson, Instrumental Methods in Electrochemistry, Horwood Publishing Limited, Chichester, 2001.
[38] T.J. Schmidt, H.A. Gasteiger, G.D. Stäb, P.M. Urban, D.M. Kolb, R.J. Behm, Journal of the Electrochemical Society 145 (1998) 2354–2358.
[39] TIMCAL Ltd. webpage: http://www.timcal.com/scopi/group/timcal/timcal.nsf/pagesref/SCMM-7EVDQM?Opendocument&lang=en.
[40] E.G. Rakov, D.A. Grishin, Yu.V. Gavrilov, E.V. Rekova, A.G. Nasibulin, H. Jiang, E.I. Kauppinen, Russian Journal of Physical Chemistry 78 (2004) 1966–1971.
[41] Timesnano webpage: http://www.timesnano.com/products/Research%20Grades_MWCNT.asp and technical data sheets downloadable from: http://www.timesnano.com/products/GM2.asp.
[42] Showa Denko K.K. webpage: http://www.sdk.co.jp/html/english/products/finecarbon/vgcf.html.
[43] Product data sheet for VULCAN® XC72, Cabot Corporation: http://www.cabot-corp.com/wcm/download/en-us/sb/VULCAN_XC72-English1.pdf.
[44] M. Carmo, A.R. dos Santos, J.G.R. Poco, M. Linardi, Journal of Power Sources 173 (2007) 860–866.
[45] J. Giner, Journal of the Electrochemical Society 111 (1964) 376–377.
[46] G. Pacchioni, A.M. Ferrari, Catalysis Today 50 (1999) 533–540.
[47] I.D. Mikheikin, I.A. Abronin, I.K. Vorontsova, Colloids and Surfaces A: Physicochemical and Engineering Aspects 115 (1996) 207–217.
[48] J.G. Castle Jr., D.C. Wobschall, Paramagnetic resonance absorption in heat-treated carbon blacks, in: S. Mrozowski, M.L. Studebaker, P.L. Walker (Eds.), Proceedings of the Third Conference on Carbon, Pergamon Press Ltd, London, 1959, pp. 129–134.
[49] A.V. Nikolaev, B. Verberck, Diamagnetism of diamond and graphite, in: T.L. Makarova, F. Palacio (Eds.), Carbon-Based Magnetism. An Overview of the Magnetism of Metal Free Carbon-Based Compounds and Materials, Elsevier B.V, Amsterdam, 2006, pp. 245–278.
[50] G.M. Arnold, Carbon 5 (1967) 33–42.
[51] M. Kosaka, T.W. Ebbesen, H. Hiura, K. Tanigaki, Chemical Physics Letters 225 (1994) 161–164.
[52] O. Chauvet, L. Forro, W. Bacsa, D. Ugarte, B. Doudin, W.A. de Heer, Physical Review B 52 (1995) R6963–R6966.
[53] O. Zhou, R.M. Fleming, D.W. Murphy, C.H. Chen, R.C. Haddon, A.P. Ramirez, S.H. Glarum, Science 263 (1994) 1744–1747.
[54] Y. Chen, J. Chen, H. Hu, M.A. Hamon, M.E. Itkis, R.C. Haddon, Chemical Physical Letters 299 (1999) 532–535.
[55] K. Tanaka, T. Sato, T. Yamabe, K. Okahara, K. Uchida, M. Yumura, H. Niino, S. Ohshima, Y. Kuriki, K. Yase, F. Ikazaki, Chemical Physics Letters 223 (1994) 65–68.
[56] H. Estrade-Szwarckopf, Carbon 42 (2004) 1713–1721.
[57] P. Chen, X. Wu, X. Sun, J. Lin, W. Ji, K.L. Tan, Physical Review Letters 82 (1999) 2548–2551.
[58] S.M.S. Kumar, J.S. Herrero, S. Irusta, K. Scott, Journal of Electroanalytical Chemistry 647 (2010) 211–221.
[59] D.-Q. Yang, E. Sacher, Langmuir 22 (2006) 860–862.
[60] K.G. Gallagher, D.T. Wong, T.F. Fuller, Journal of The Electrochemical Society 155 (2008) B488–B493.
[61] K. Horita, Y. Nishibori, T. Ohshima, Carbon 34 (1996) 217–222.
[62] Z. Jusys, J. Kaiser, R.J. Behm, Electrochimica Acta 49 (2004) 1297–1305.